ACS APPLIED MATERIALS & INTERFACES
Research Article
www.acsami.org

Carbon and RuO_2 Binary Surface Coating for the $Li_3V_2(PO_4)_3$ Cathode Material for Lithium-Ion Batteries

Rongyu Zhang,[†] Yongquan Zhang,[†] Kai Zhu,[†] Fei Du,[†] Qiang Fu,[†] Xu Yang,[†] Yuhui Wang,[†] Xiaofei Bie,[†] Gang Chen,[†,‡] and Yingjin Wei*[,†]

[†]Key Laboratory of Physics and Technology for Advanced Batteries (Ministry of Education), College of Physics, Jilin University, Changchun 130012, People's Republic of China

[‡]State Key Laboratory of Superhard Materials, Jilin University, Changchun 130012, People's Republic of China

ABSTRACT: RuO_2 nanocrystals are successfully impregnated into the surface carbon layer of the $Li_3V_2(PO_4)_3$/C cathode material by the precipitation method. Transmission electron microscopy shows that the RuO_2 particles uniformly embed in the surface carbon layer. Cyclic voltammetry and electrochemical impedance spectroscopy indicate that the coexistence of carbon and RuO_2 enables high conductivity for both Li ions and electrons and thus stabilizes the interfacial properties of the electrode, facilitates the charge transfer reactions, and improves the Li^+ diffusion in the electrode. As a result, the $Li_3V_2(PO_4)_3$ cathode coated with the binary surface layer shows improved rate capability and cycle stability. Particularly, the material containing 2.4 wt % Ru exhibits the best electrochemical performance and delivers a discharge capacity of 106 mAh g^{-1} at the 10 C rate with a capacity retention of 98.4% after 100 cycles.

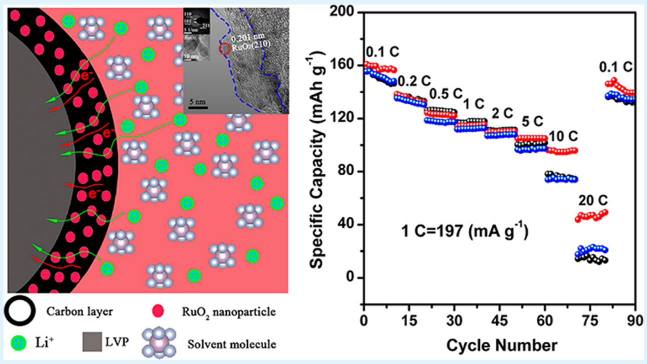

KEYWORDS: *lithium-ion battery, lithium vanadium phosphate, ruthenium dioxide, surface coating, charge−discharge cycling, rate performance*

1. INTRODUCTION

Lithium-ion batteries have conquered the consumer market of portable electronics and are now being considered as power sources for electric vehicles and energy storage systems for smart grids. Most commercial Li-ion batteries use $LiCoO_2$ as the cathode material. But the high cost, toxic properties, and safety problem of $LiCoO_2$ hamper its practical applications in large-format Li-ion batteries. Recently, lithium-based phosphates such as $LiMPO_4$ (M = Co, Mn, Fe)[1−4] and $Li_3M_2(PO_4)_3$ (M = V, Fe)[5−7] have been proposed as the next generation of cathode materials. The framework of these polyanion materials is constructed by a rigid $[PO_4]^{3-}$ network, which helps to stabilize the crystal structure of the materials. The oxygen atoms are fixed in the $[PO_4]^{3-}$ structure. This limits the likelihood of oxygen liberation, which leads to good thermal stability. In addition, incorporation of the $[PO_4]^{3-}$ groups also raises the working voltage of the materials by the "inductive effect".[8]

Among various polyanion cathode materials, monoclinic $Li_3V_2(PO_4)_3$ (LVP) has the largest theoretical capacity, 197 mAh g^{-1}, on the basis of three Li^+ extractions from the material lattice. LVP crystallizes in a NASICON structure, which has the ability to facilitate Li^+ diffusion. However, like most polyanion materials, the separated $[VO_6]$ octahedral reduces the electronic conductivity of LVP, which is an intrinsic drawback for its electrochemical performance. Numerous works have been done to resolve the above problem, including surface coating or mixing with highly conductive materials,[9−12] reducing particle size,[13−15] controlling morphology,[16,17] and doping with foreign atoms.[18−20] Among various approaches, carbon coating has been proven to be effective. On one hand, the surface carbon layer can effectively retard the growth of the LVP particles, which favors Li^+ insertion due to the shortened Li^+ diffusion distance and the increased contact area with electrolyte. On the other hand, the surface carbon layer can dramatically improve the electronic conductivity of the LVP particles and decrease the polarization of the electrode, resulting in a significantly improved rate performance.

Even though carbon coating has shown multiple functions in improving the electrochemical properties of LVP, it still has some challenges and limitations. First, the effectiveness of carbon coating is affected by many factors such as the weight ratio, conductivity, thickness, coating uniformity, and so on.[21] In spite of its excellent electronic conductivity, LVP is not a good ionic conductor. A carbon layer that is too thick will act as a barrier for Li^+ diffusion, thus limiting the electrochemical performance of the material, especially at high charge−discharge rates.

Received: April 22, 2014
Accepted: July 7, 2014
Published: July 10, 2014

dx.doi.org/10.1021/am502387z | *ACS Appl. Mater. Interfaces* 2014, 6, 12523−12530

Instead, the so-called hybrid surface coating that combines different coating species might be an alternative to the conventional carbon coating technique. The concept of "hybrid surface coating" was first proposed by Zhou et al.[21] The electrochemical performance of carbon coated cathode materials (e.g., $LiFePO_4$) is expected to be improved by such a hybrid surface coating via the synergetic effects of the surface carbon layer and the secondary coating species. For example, Choi et al. prepared LVP/Ag + graphene composite cathode. The material showed excellent electrochemical properties due to the effective electron transport network constructed by Ag and graphene.[22] Zhang et al. prepared LVP/C + SiO_2 cathode material. The improved electrochemical properties were attributed to the enhanced structural stability and reduced charge-transfer resistance of the material.[23] In this work, we construct a novel hybrid surface coating for LVP in which the amorphous carbon acts as the main body of the coating layer, which improves the electronic conductivity of the material, while a nanosized secondary phase with good Li-ion conductivity is impregnated into the carbon coating, thus enabling high conductivity for both Li ions (Li^+) and electrons (e^-) (Scheme 1). Various Li-ion conductors, such as Li_3PO_4 ($\sim10^{-6}$ S m^{-1}),[24] Li_3VO_4 ($\sim10^{-4}$ S m^{-1}),[25] and RuO_2 ($\sim10^{-8}$ S m^{-1}), can be considered as the secondary phase.[26] Here, we do not use Li_3PO_4 and Li_3VO_4 due to their poor electronic conductivity. We specifically choose RuO_2 not only because it is a suitable Li-ion conductor but also because its high electronic conductivity will not compromise the high conductivity of the surface carbon layer. This work demonstrates that the LVP cathode material coated with the C + RuO_2 hybrid surface layer shows improved electrochemical performance with respect to that of carbon-coated LVP.

Scheme 1. C + RuO_2 Binary Surface Coating for the LVP Cathode

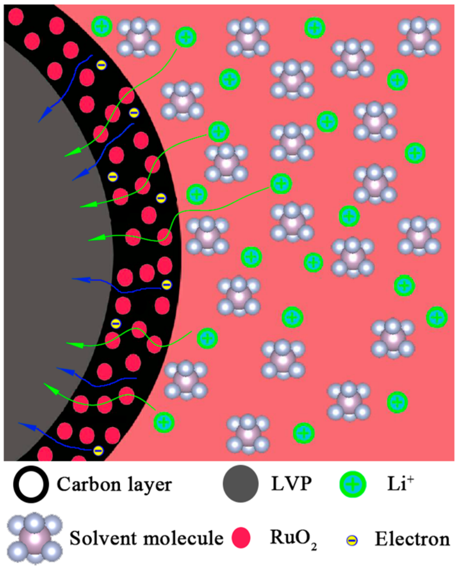

2. EXPERIMENTAL SECTION

Carbon-coated LVP (LVP/C) was prepared by the conventional carbothermal reduction (CTR) method. Li_2CO_3, $NH_4H_2PO_4$, and NH_4VO_3 were used as the starting materials. Sucrose ($C_{12}H_{22}O_{11}$) was employed as the carbon source. Stoichiometric Li_2CO_3, $NH_4H_2PO_4$, and NH_4VO_3, together with 16 wt % sucrose powder, were mixed by ball milling. The mixture was first treated at 300 °C under N_2 flow for 4 h. The resulting powder was then pressed into a tablet, followed by heat treatment at 800 °C for 8 h under N_2 flow. The as-obtained LVP/C was further used to prepare the C + RuO_2 coated LVP (LVP/C + RuO_2) samples. As a typical procedure, LVP/C and a certain amount of $RuCl_3{\cdot}xH_2O$ were dispersed into distilled water under vigorous stirring. Then, 0.1 mol L^{-1} NaOH was dropped into the solution to keep the pH value at 8−9. At this condition, a controlled precipitation reaction occurred, and ruthenium hydroxide formed on the surface of the LVP/C particles. After the precipitation process, the product was washed completely to remove the residual chloride. Finally, the clean precipitate was heat treated at 450 °C under N_2 flow for 3 h to obtain the desired LVP/C + RuO_2 samples.

Powder X-ray diffraction (XRD) was performed on a Rigaku AXS D8 X-ray diffractometer with Cu Kα radiation at a scan rate of 0.01° s^{-1}. Raman scattering was recorded on a Renishaw inVia Raman microscope with Ar-ion laser excitation. X-ray photoelectron spectroscopy (XPS) was conducted on a VG scientific ESCALAB 250 spectrometer using a monochromic Al Kα excitation. The binding energies were calibrated with the C 1s peak at 284.71 eV. Scanning electron microscopy (SEM) was performed on a JEOL JSM-6700F microscope operated with an accelerating voltage of 20 kV. High-resolution transmission electron microscopy (HRTEM) was performed on an FEI Tecnai G2 F20 S-TWIN microscope equipped with an X-ray energy dispersive spectroscopy (EDS, Bruker AXS). Thermogravimetric analysis (TGA) was performed on an SDTA851E thermoanalyzer between room temperature and 800 °C with a heating rate of 10 °C min^{-1} under O_2 flow.

Electrochemical properties of the samples were studied with CR2032 coin cells between 4.8 and 3.0 V using metallic lithium as the anode electrode. For preparing the cathode electrode, a slurry mixture containing 75 wt % active material, 15 wt % super P conductive additive, and 10 wt % polyvinyl difluoride (PVDF) binder was pasted on an Al foil and dried in vacuum at 120 °C. The electrode was cut into a size of 8 × 8 mm^2 and contained about 2.0 mg of active material. The electrolyte was a 1 M $LiPF_6$ solution dissolved in ethylene carbonate (EC), dimethyl carbonate (DMC), and ethylmethyl carbonate (EMC), with EC/DMC/EMC = 1:1:1 by v/v ratio. The cathode and anode electrodes were separated by a Celgard 2320 membrane. Galvanostatic charge−discharge was performed in the voltage window of 3.0−4.8 V on a Land automatic battery tester. Cyclic voltammetry (CV) and electrochemical impedance spectroscopy (EIS) were collected on a Bio-Logic VSP multichannel potentiostatic−galvanostatic electrochemical workstation. The CV measurement was performed in the voltage window of 3.0−4.8 V. The EIS data was obtained over a frequency range between 1 MHz and 1 mHz by applying an ac voltage of 5 mV.

3. RESULTS AND DISCUSSION

3.1. Structure and Morphology Characterizations. The LVP/C sample is prepared by the CTR method using sucrose as the carbon source. During the high-temperature heat treatment, the sucrose will be carbonized. A part of the carbon is consumed to reduce the V^{5+} ions in the NH_4VO_3 raw material to V^{3+}, while the rest will coat the surface of the LVP particles. To determine the carbon content in LVP/C, we carried out TGA by heating the LVP/C sample under O_2 flow. As shown in Figure 1, the gradual weight loss of 3.5 wt % before 370 °C is due to the evaporation of absorbed and chemically bonded water in the sample. The abrupt weight loss between 370 and 530 °C is attributed to the combustion of residual carbon,[2] indicating that the carbon content in the material is 8.3 wt %. In addition, the carbon content was measured by dissolving the LVP/C sample in hydrochloric acid using ultrasonic dispersion. The undissolved carbon was weighed using a microbalance and is found to be 7.97 wt %, which fit well with that of the TGA result.

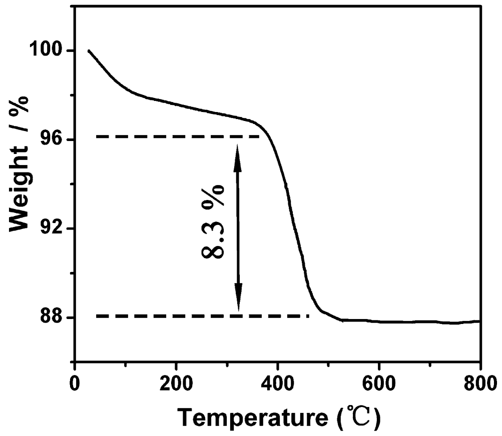

Figure 1. TGA curve of the LVP/C sample.

Figure 2 shows the Rietveld refinement results of the XRD patterns of the LVP/C and LVP/C + RuO_2 samples. All the patterns can be perfectly refined on the basis of monoclinic $Li_3V_2(PO_4)_3$ with space group of $P2_1/n$. This indicates that incorporation of RuO_2 and carbon does not change the crystal structure of LVP. No diffractions from RuO_2 and carbon are observed due to the amorphous nature of the residual carbon and the small particles of RuO_2, as will be shown by HRTEM. Table 1 shows the calculated lattice parameters of the samples. All the samples have very similar lattice parameters, indicating that no Ru ions are doped in the LVP lattice.

SEM and HRTEM were performed to study the morphology and microstructure of the materials. As shown in Figure 3, there is no significant difference between the SEM images of LVP/C and LVP/C + RuO_2. The particles of the samples show irregular shapes with some agglomeration and a wide size distribution ranging from 500 nm to 1 μm. Figure 4 shows the HRTEM images of the three samples. The LVP/C sample shows an amorphous surface carbon layer with a thickness of about 7 nm. In the material bulk, the lattice fringes with an interplannar distance of 3.67 Å correspond to the *d*-spacing of the (112) planes of LVP. In addition, the indexed selected area electron diffraction (SAED) pattern confirms that the monoclinic $Li_3V_2(PO_4)_3$ phase is successfully formed. The LVP/C + RuO_2 samples also have a surface carbon layer similar to that of LVP/C. But there are numerous nanoparticles (~2 nm) embedding in the carbon layer. The lattice fringes of the nanoparticles have an interplannar distance of 2.01 Å, which corresponds to the *d*-spacing of the (210) planes of RuO_2. To further confirm the formation of RuO_2, we prepared RuO_2 particles using the same precipitation procedure described in the Experimental Section. HRTEM image shows that the resultant powders are composed of nanoparticles. The corresponding SAED pattern shows a series of rings that can be indexed to the RuO_2 phase. The existence of Ru in the LVP/C + RuO_2 samples is also confirmed by EDS mapping, as shown in Figure 5. It shows that the Ru element uniformly distributes in the samples, which are measured to be 2.4 (sample b) and 5.1 wt % (sample c). (Note that the LVP/C sample is denoted as sample a in this work.) Additionally, one can see from HRTEM that the thickness of the surface carbon layer increases slightly to ~8 nm after the addition of RuO_2. This indicates that the embedded RuO_2 nanoparticles expand the volume of the surface carbon layer.

Table 1. Lattice Parameters of the LVP/C and LVP/C + RuO_2 Samples

sample	*a* (Å)	*b* (Å)	*c* (Å)	*β* (deg)	*V* (Å^3)
a	8.6192	8.6083	12.0595	90.540	894.73
b	8.6204	8.6094	12.0572	90.360	894.81
c	8.6186	8.6106	12.0533	90.350	894.45

Figure 6 shows the Raman patterns of the LVP/C and LVP/C + RuO_2 samples. All the patterns show two broad peaks at around 1593 and 1360 cm^{-1}, which are due to the G and D bands of carbonaceous materials, respectively. Monoclinic LVP has a series of Raman bands between 800 and 1200 cm^{-1} that mainly arise from the [PO_4] groups.[27] However, it is difficult to distinguish these Raman bands from the present Raman patterns, because the highly conductive surface carbon layer absorbs most of the incident photons so that the penetration depth inside the material bulk is too short to be effective for data collection.[6,15,23] On the other hand, even though some weak Raman signals from [PO_4] groups can be obtained, they can easily overlap with the D band of the surface carbon layer. The G band of carbonaceous materials is due to the E_{2g} zone-center mode of crystalline graphite, and the D band is attributed to the A_{1g} mode that relates to the breakage of symmetry at the edges of graphite sheets. The relative intensity of the D and G bands, I_D/I_G, provides useful information on the graphite crystalline of carbonaceous materials. By comparing the I_D/I_G values of the materials (i.e., 0.99 for sample a, 0.98 for sample b, and 0.98 for sample c), it is seen that the RuO_2 secondary phase does not affect the graphite crystalline of the surface carbon.

3.2. X-Ray Photoelectron Spectroscopy. XPS is performed to study the surface chemistry of the LVP/C and LVP/C + RuO_2 samples. Full-scale XPS confirms the existence of Li, V, P, and O elements in all samples. Additional signals from Ru are obtained for the LVP/C + RuO_2 samples. The oxidation state of Ru is determined from the Ru 3d XPS as shown in Figure 7a. The spectra display the characteristic shape

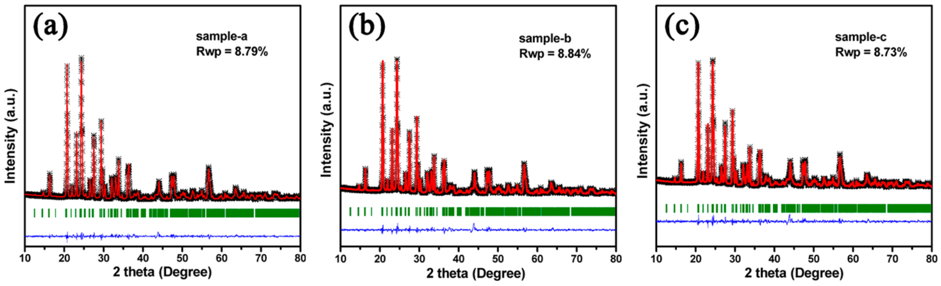

Figure 2. (a−c) Rietveld refinement of the XRD patterns of the LVP/C and LVP/C + RuO_2 samples.

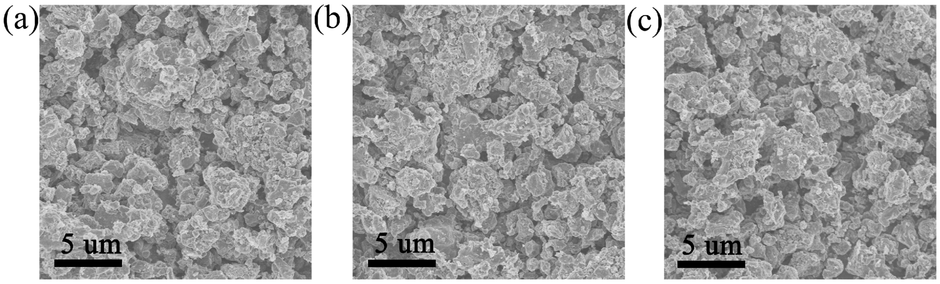

Figure 3. SEM images of (a) sample a, (b) sample b, and (c) sample c.

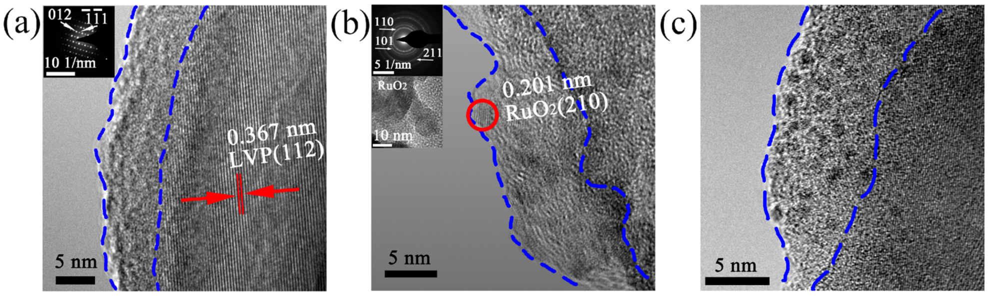

Figure 4. HRTEM images of (a) sample a, (b) sample b, and (c) sample c. (a, Inset) SAED pattern of sample-a, (b, Inset) SAED pattern and HRTEM image of RuO_2 nanoparticles.

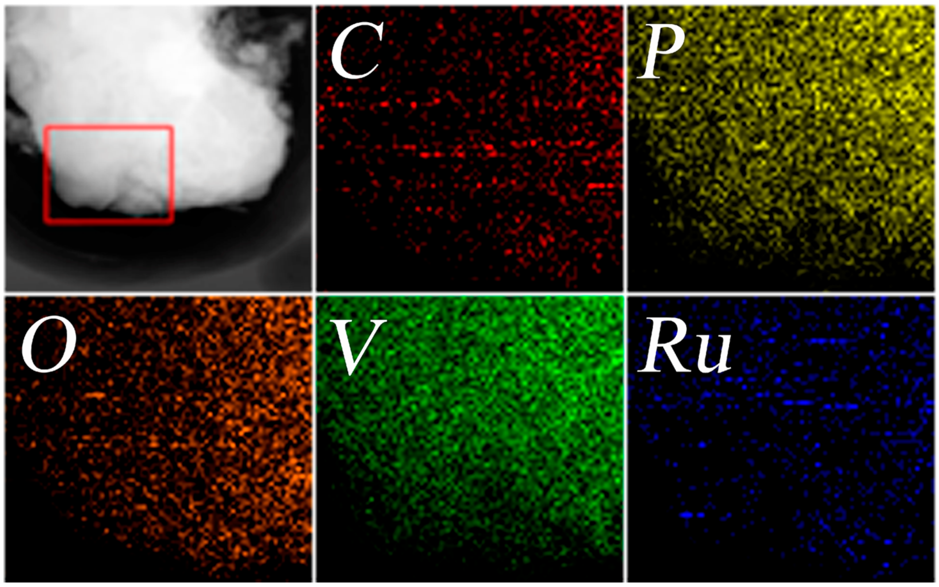

Figure 5. EDX mapping of the LVP/C + RuO_2 sample (sample b).

of the Ru 3d doublet, showing two peaks corresponding to the 5/2 and 3/2 spin orbit components. The Ru $3d_{5/2}$ peak, which does not overlap with the Ru $3d_{3/2}$ and C 1s peaks, appears at 280.5 eV. This binding energy corresponds to that of Ru^{4+} ions reported in the literature.[28,29] Figure 7b shows that the V 2p XPS of LVP/C is very similar to that of LVP/C + RuO_2 samples, where the peaks at 516.9 and 523.8 eV are due to the V $2p_{3/2}$ and V $2p_{1/2}$ doublets, respectively. The binding energies are consistent with those of V^{3+} in $Li_3V_2(PO_4)$,[30,31] which indicates that RuO_2 does not change the oxidation state of V in the materials.

3.3. Cyclic Voltammetry. Figure 8 displays the CV curves of the samples at varies scan rates. The CV curves show four current peaks in the anodic branch, which are labeled as a, b, c, and d, corresponding to the two-phase transitions between the $Li_xV_2(PO_4)_3$ phases (x = 2.5, 2.0, 1.0, and 0). During the following cathodic process, the a and b peaks are well reversible (a/a″ and b/b′), but the c and d peaks emerge into a single peak of c′, which is attributed to the solid solution region from $V_2(PO_4)_3$ to $Li_2V_2(PO_4)_3$.[23] The LVP/C + RuO_2 samples exhibit more symmetrical and sharper current peaks than LVP/C. Furthermore, the anodic peaks shift left and the cathodic peaks shift right with respect to those of LVP/C, suggesting smaller polarization of the LVP/C + RuO_2 electrodes. Table 2 shows that the electrode polarization decreases with the addition of 2.4 wt % Ru and then slightly increases with the increase of Ru content to 5.1 wt %, except for the a/a′ redox couple. This indicates that too much RuO_2 is not good for the electrochemical reversibility of the LVP active material.

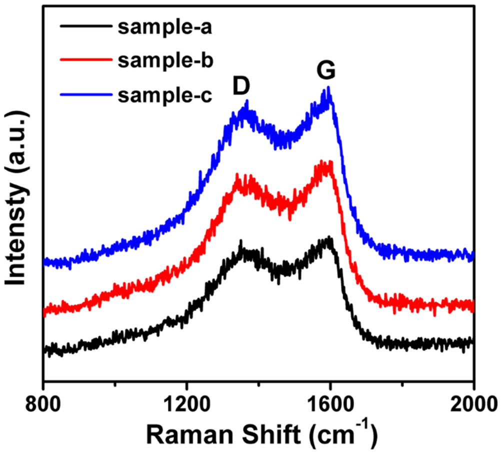

Figure 6. Raman spectra of the LVP/C and LVP/C + RuO_2 samples.

CV has been used to determine the Li^+ diffusion coefficients (D_{Li}) of electrode materials through the following equation:[32]

$$I_p = 2.69 \times 10^5 n^{3/2} A D^{1/2} v^{1/2} C \quad (1)$$

where n is the number of electrons per species reaction (for Li^+, $n = 1$); A is the surface area of the electrode (0.64 cm^2 in this work); and C is the concentration of Li ions in the electrode (e.g., 1.1×10^{-2} mol cm^{-3} at peak c where the chemical composition of the active material is $Li_{1.5}V_2(PO_4)_3$). I_p is the current intensity, and v is the scan rate. At relatively low scan rates, Li ions accumulate in the active material, and thus, I_p varies linearly with $v^{1/2}$, as shown in the inset of Figure 8. On this basis, one can calculate the lithium diffusion coefficients using eq 1. Table 3 lists the D_{Li} values of the samples at peaks c and c′. Among the three samples, sample b, which contains 2.4 wt % Ru, has the largest Li-ion diffusion coefficients, which implies its good electrochemical performance and especially its rate capability.

3.4. Charge−Discharge Cycling. Galvonostatic charge−discharge experiments are performed on the LVP/C and LVP/C + RuO_2 samples in a voltage range of 3.0−4.8 V. Figure 9 displays the voltage profiles of the materials at various current rates increasing from 0.5 C (98.5 mA g^{-1}) to 20 C (3940 mA g^{-1}). The slope-like curve between 4.8 and 3.7 V is due to the solid solution region from $V_2(PO_4)_3$ to $Li_2V_2(PO_4)_3$. The plateaus at ~3.6 and 3.55 V are due to the two-phase transitions from $Li_2V_2(PO_4)_3$ to $Li_{2.5}V_2(PO_4)_3$ and from $Li_{2.5}V_2(PO_4)_3$ to $Li_3V_2(PO_4)_3$, respectively. The electrode polarization becomes larger with the increase of current rate due to the limitation of electrochemical kinetics. Figure 10 shows the rate-dependent cycling performance of the samples. The discharge capacities of the three samples do not show significant differences when the current rate is lower than 2 C. However, the rate performance of sample b becomes much better than the other samples when the current rate is increased to 5 C. The material shows a high discharge capacity of 96.3 mAh g^{-1} at the 10 C rate, which is much higher than that of 78.2 mAh g^{-1} for LVP/C. When the charge−discharge rate is increased to 20 C, it still shows a discharge capacity of 48.2 mAh g^{-1}. When the current rate is returned to 0.1 C, the discharge capacities of the three samples all return to their initial states, indicating good electrochemical reversibility of the materials. Furthermore, we study the cycling performance of the samples at the 10 C rate, as shown in Figure 11. The discharge capacity of sample c shows a slight increase in the first 10 cycles, which could be due to the continuous activation of the electrode in the initial electrochemical process. For samples a, b, and c, the largest discharge capacities are 73.9, 102.5, and 98.6 mAh g^{-1}, respectively, and the capacity retention after 100 cycles are 89.6, 98.5, and 94.5%, respectively. Sample b, which contains 2.4 wt % Ru, exhibits the largest discharge capacity and the best cycle stability among the three samples.

3.5. Electrochemical Impedance Spectroscopy. Electrochemical impedance spectroscopy of the samples is carried out after 1 and 20 cycles at a charge of 4.8 V. Figure 12 shows the Nyquist plots of the materials. The high frequency intercept at the Z_{real} axis corresponds to the ohmic resistance of the cell, which contains the resistance of electrolyte, separator, current collector, and so on. The inclined line in the low frequency region represents the Li^+ diffusion in the electrode bulk. The semicircle in the middle frequency range is attributed to the solid electrolyte interface (SEI) film and the charge transfer process. The formation of SEI film on LVP/C has been clearly observed under HRTEM in our previous work.[30] However, it is hard to distinguish the SEI film and the charge transfer process from the present Nyquist plots, perhaps because the two components have similar time constants. To be as general as possible in this work, we refer to the resistance obtained from the semicircle as the interfacial resistance. EIS shows that sample b exhibits the lowest interfacial resistance of 87.2 Ω after the first charge, while sample a shows the largest interfacial resistance of 191.6 Ω. More importantly, the interfacial resistances of the LVP/C + RuO_2 samples remain very stable

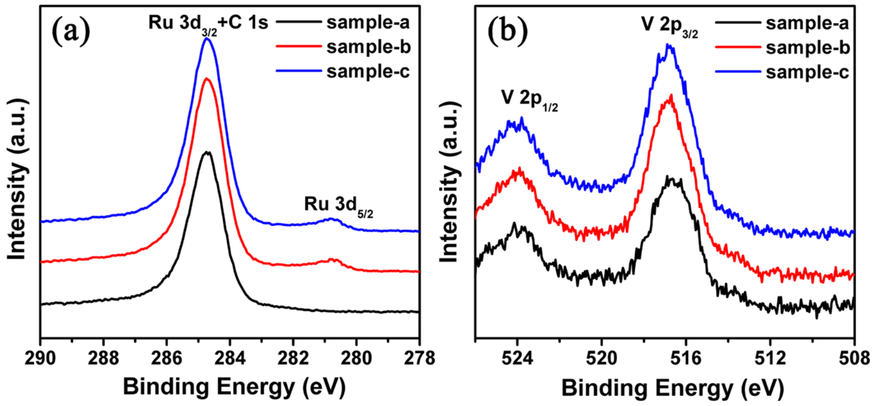

Figure 7. (a) C 1s + Ru 3d and (b) V 2p XPS of the LVP/C and LVP/C + RuO_2 samples.

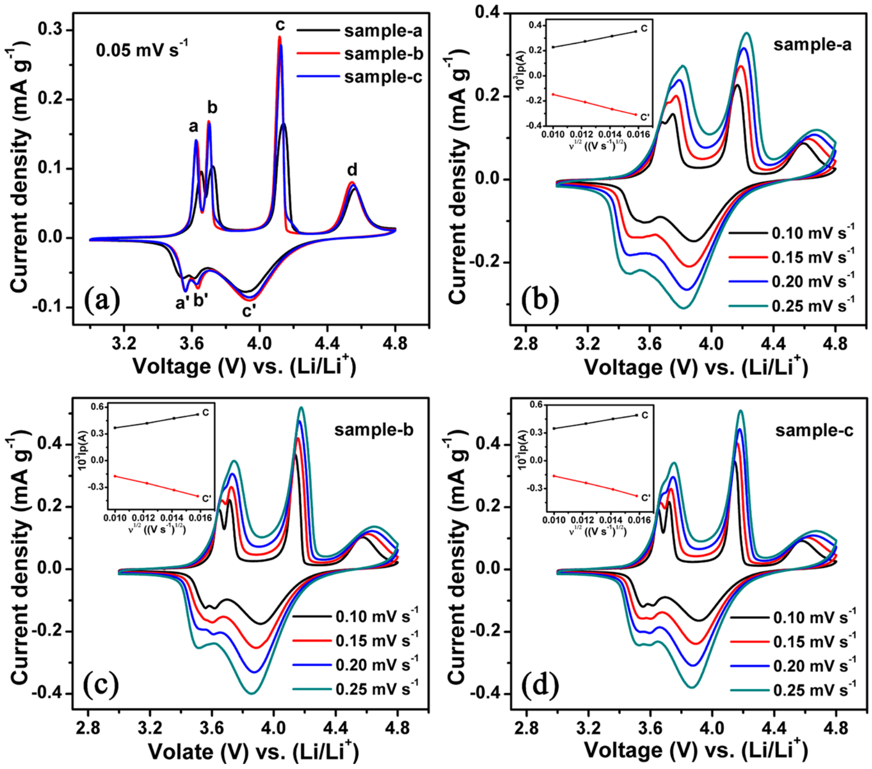

Figure 8. (a) CV curves of the LVP/C and LVP/C + RuO_2 samples at a scan rate of 0.05 mV s^{-1}; (b–d) CV curves of the LVP/C and LVP/C + RuO_2 samples at different scan rates; and (insets) linear fitting of the I_p versus $v^{1/2}$ relationships.

Table 2. Electrode Polarizations of the LVP/C and LVP/C + RuO_2 Samples at a CV Scan Rate of 0.05 mV s^{-1}

sample	$\Delta E_{a-a'}$ (V)	$\Delta E_{b-b'}$ (V)	$\Delta E_{c-c'}$ (V)	$\Delta E_{d-c'}$ (V)
a	0.11	0.11	0.22	0.64
b	0.07	0.06	0.17	0.60
c	0.06	0.08	0.18	0.61

Table 3. Lithium Diffusion Coefficients of the LVP/C and LVP/C+RuO_2 Samples

	sample a	sample b	sample c
peak *c* (cm^2 s^{-1})	1.58×10^{-10}	2.31×10^{-10}	2.09×10^{-10}
peak *c′* (cm^2 s^{-1})	2.61×10^{-10}	5.06×10^{-10}	4.58×10^{-10}

with charge–discharge cycling, but that of LVP/C increases to 395.8 Ω after 20 cycles. This indicates that the interfacial properties of the LVP electrode are stabilized by the C + RuO_2 binary surface coating.

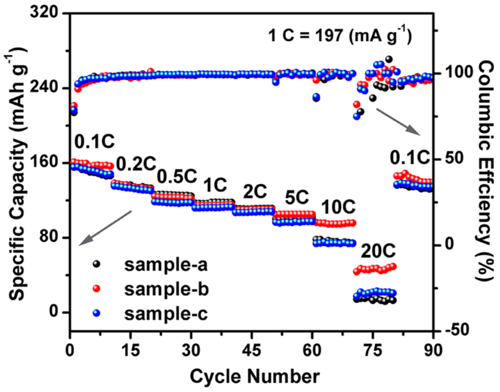

Figure 10. Rate-dependent cycling performance of the LVP/C and LVP/C + RuO_2 samples.

The intrinsic low electronic conductivity of LVP has enabled researchers to prepare carbon coated LVP cathode materials. Normally, the surface carbon layer is amorphous, which allows

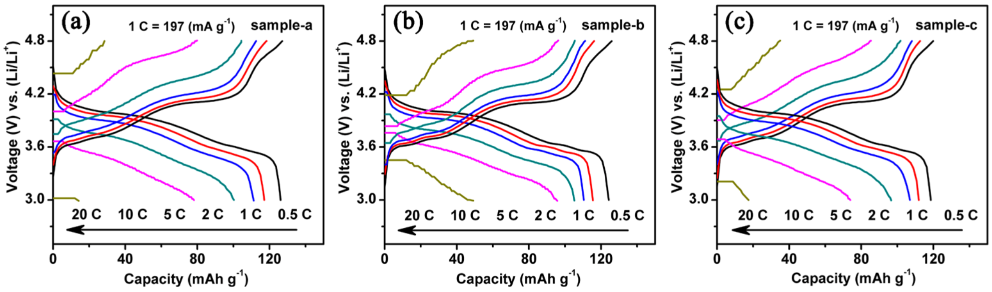

Figure 9. (a–c) Voltage profiles of the LVP/C and LVP/C + RuO_2 samples at various current rates.

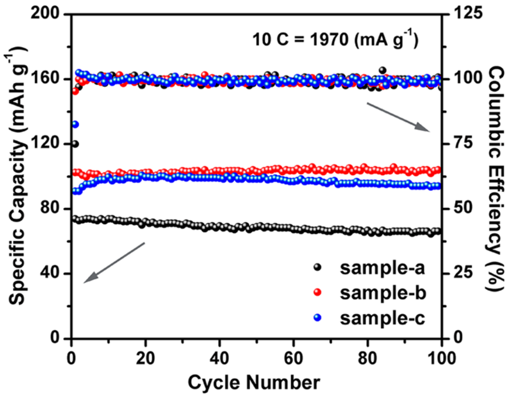

Figure 11. Cycling performance of the LVP/C and LVP/C + RuO_2 samples at the 10 C rate.

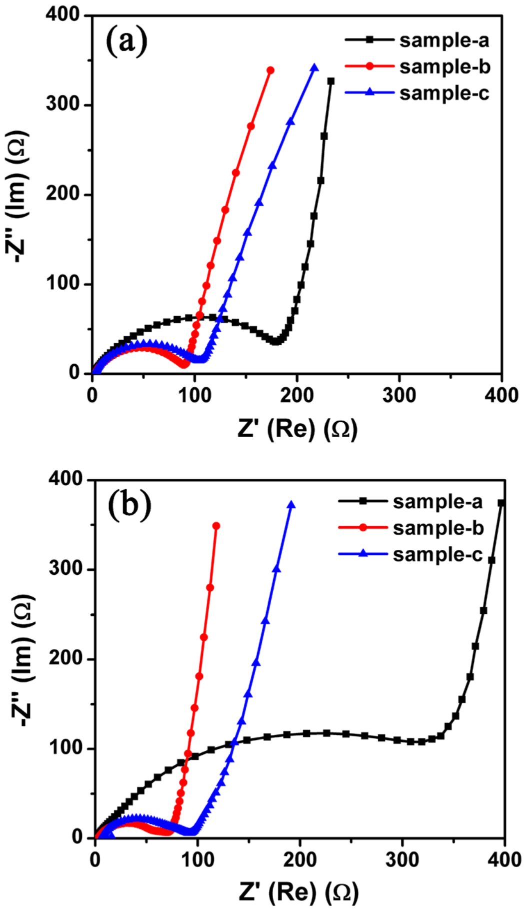

Figure 12. Nyquist plots of the LVP/C and LVP/C + RuO_2 samples (a) after 1 cycle and (b) after 20 cycles.

the electrolyte to penetrate. At relatively low current rates, both the electrons (e^-) and Li ions (Li^+) can effectively transport through the surface carbon layer, thus fulfilling the charge transfer reactions. At high current rates, the current flow increases, which correspondingly requires simultaneous Li^+ transportation in the surface layer to ensure effective charge transfer reactions. However, in spite of its high electronic conductivity, carbon is not a good ionic conductor. It will act as a barrier for Li^+ diffusion and thus limit the electrochemical performance of the material, especially at high current rates. Therefore, a threshold of the rate performance (5 C for the present LVP/C cathode) is observed for the electrode. To improve the rate performance of the LVP/C cathode, we propose introducing a secondary phase that possesses high ionic conductivity into the surface carbon layer. In such a hybrid surface coating, the amorphous carbon acts as the main body of the surface coating, which improves the electronic conductivity of the material, while the secondary phase with good Li-ion conductivity is embedded in the carbon coating. During electrochemical processes, the Li ions can pass through the surface layer quickly via the Li_xRuO_2 medium phase (σ_{Li} = ~10^{-8} S cm^{-1}).[26] Meanwhile, the electrons transport through the surface carbon layer, fulfilling the simultaneous Li^+/electron charge transfer. This synergetic effect of the C + RuO_2 binary surface coating is more significant at high charge−discharge rates above 5 C. However, too much RuO_2 in the binary surface coating is not accepted because the nanosized RuO_2 crystals prohibit the penetration of electrolyte. This work shows that 2.4 wt % Ru is a proper amount for the present LVP/C cathode, which can effectively improve the high rate performance of $Li_3V_2(PO_4)_3$ cathode.

4. CONCLUSIONS

In summary, nanosized RuO_2 secondary phase was successfully impregnated into the surface carbon layer of the LVP/C cathode by the precipitation method. The coexistence of carbon and RuO_2 in the surface layer enables high conductivity for both Li ions and electrons and thus facilitates the charge transfer reactions at the electrode interface and the Li^+ diffusion in the electrode bulk. Additionally, this binary surface coating stabilizes the interfacial properties of the LVP cathode. As a result, the LVP cathode coated with the C + RuO_2 binary surface layer shows good electrochemical performance in terms of high rate capability and cycle stability.

■ AUTHOR INFORMATION

Corresponding Author

*E-mail: yjwei@jlu.edu.cn. Tel. and Fax: 86-431-85155126.

Notes

The authors declare no competing financial interest.

■ ACKNOWLEDGMENTS

This work was supported by the National Natural Science Foundation of China (Grant No. 51272088), the Defense Industrial Technology Development Program (Grant No. B1420133045), the Research Fund for the Doctoral Program of Higher Education of China (Grant No. 20110061130006), and the Research Fund for High Technology Development of Jilin Province (Grant No. 20120310).

■ REFERENCES

(1) Truong, Q. D.; Devaraju, M. K.; Tomai, T.; Honma, I. Direct Observation of Antisite Defects in $LiCoPO_4$ Cathode Materials by Annular Dark- and Bright-Field Electron Microscopy. *ACS Appl. Mater. Interfaces* **2013**, *5*, 9926−9932.

(2) Zhang, L. F.; Qu, Q. T.; Zhang, L.; Li, J.; Zheng, H. H. Confined Synthesis of Hierarchical Structured $LiMnPO_4$/C Granules by a Facile Surfactant-Assisted Solid-State Method for High-Performance Lithium-Ion Batteries. *J. Mater. Chem. A* **2014**, *2*, 711−719.

(3) Wang, J. J.; Yang, J. L.; Tang, Y. J.; Li, R. Y.; Liang, G. X.; Sham, T. K.; Sun, X. L. Surface Aging at Olivine $LiFePO_4$: A Direct Visual Observation of Iron Dissolution and the Protection Role of Nano-Carbon Coating. *J. Mater. Chem. A* **2013**, *1*, 1579−1586.

(4) Ravnsbæk, D. B.; Xiang, K.; Xing, W.; Borkiewicz, O. J.; Wiaderek, K. M.; Gionet, P.; Chapman, K. W.; Chupas, P. J.; Chiang, Y. M. Extended Solid Solutions and Coherent Transformations in Nanoscale Olivine Cathodes. *Nano Lett.* **2014**, *14*, 1484−1491.

(5) Li, D. L.; Tian, M.; Xie, R.; Li, Q.; Fan, X. Y.; Gou, L.; Zhao, P.; Ma, S. L.; Shi, Y. X.; Yong, H. T. H. Three-Dimensionally Ordered Macroporous $Li_3V_2(PO_4)_3/C$ Nanocomposite Cathode Material for High-Capacity and High-Rate Li-Ion Batteries. *Nanoscale* **2014**, *6*, 3302−3308.

(6) Wei, Q. L.; An, Q. Y.; Chen, D. D.; Mai, L. Q.; Chen, S. Y.; Zhao, Y. L.; Hercule, K. M.; Xu, L.; Minhas-Khan, A.; Zhang, Q. J. One-Pot Synthesized Bicontinuous Hierarchical $Li_3V_2(PO_4)_3/C$ Mesoporous Nanowires for High-Rate and Ultralong-Life Lithium-Ion Batteries. *Nano Lett.* **2014**, *14*, 1042−1048.

(7) Karami, H.; Taala, F. Synthesis, Characterization and Application of $Li_3Fe_2(PO_4)_3$ Nanoparticles as Cathode of Lithium-Ion Rechargeable Batteries. *J. Power Sources* **2011**, *196*, 6400−6411.

(8) Yamada, A.; Chung, S. C.; Hinokuma, K. Optimized $LiFePO_4$ for Lithium Battery Cathodes. *J. Electrochem. Soc.* **2001**, *148*, 224−229.

(9) Xun, S. D.; Chong, J.; Song, X. Y.; Liu, G.; Battaglia, V. S. $Li_4P_2O_7$ Modified High Performance $Li_3V_2(PO_4)_3$ Cathode Material. *J. Mater. Chem.* **2012**, *22*, 15775−15781.

(10) Wang, S. L.; Zhang, Z. X.; Jiang, Z. T.; Deb, A.; Yang, L.; Hirano, S. I. Mesoporous $Li_3V_2(PO_4)_3$@CMK-3 Nanocomposite Cathode Material for Lithium Ion Batteries. *J. Power Sources* **2014**, *253*, 294−299.

(11) Pei, B.; Jiang, Z. Q.; Zhang, W. X.; Yang, Z. H.; Manthiram, A. Nanostructured $Li_3V_2(PO_4)_3$ Cathode Supported on Reduced Graphene Oxide for Lithium-Ion Batteries. *J. Power Sources* **2013**, *239*, 475−482.

(12) Jiang, T.; Wei, Y. J.; Pan, W. C.; Li, Z.; Ming, X.; Chen, G.; Wang, C. Z. Preparation and Electrochemical Studies of $Li_3V_2(PO_4)_3$/Cu Composite Cathode Material for Lithium Ion Batteries. *J. Alloys Compd.* **2009**, *488*, L26−L29.

(13) Qiao, Y. Q.; Tu, J. P.; Xiang, J. Y.; Wang, X. L.; Mai, Y. J.; Zhang, D.; Liu, W. L. Effects of Synthetic Route on Structure and Electrochemical Performance of $Li_3V_2(PO_4)_3/C$ Cathode Materials. *Electrochim. Acta* **2011**, *56*, 4139−4145.

(14) Li, Y. Z.; Liu, X.; Yan, J. Study on Synthesis Routes and their Influences on Chemical and Electrochemical Performances of $Li_3V_2(PO_4)_3$/Carbon. *Electrochim. Acta* **2007**, *53*, 474−479.

(15) Rui, X. H.; Sim, D. H.; Wong, K. M.; Zhu, J. X.; Liu, W. L.; Xu, C.; Tan, H. T.; Xiao, N.; Hng, H. H.; Lim, T. M.; Yan, Q. $Li_3V_2(PO_4)_3$ Nanocrystals Embedded in a Nanoporous Carbon Matrix Supported on Reduced Graphene Oxide Sheets: Binder-Free and High-Rate Cathode Material for Lithium-Ion Batteries. *J. Power Sources* **2012**, *214*, 171−177.

(16) Qiao, Y. Q.; Tu, J. P.; Wang, X. L.; Zhang, D.; Xiang, J. Y.; Mai, Y. J.; Gu, C. D. Synthesis and Improved Electrochemical Performances of Porous $Li_3V_2(PO_4)_3/C$ Spheres as Cathode Material for Lithium-Ion Batteries. *J. Power Sources* **2011**, *196*, 7715−7720.

(17) Liu, H. W.; Cheng, C. X.; Huang, X. T.; Li, J. L. Hydrothermal Synthesis and Rate Capacity Studies of $Li_3V_2(PO_4)_3$ Nanorods as Cathode Material for Lithium-Ion Batteries. *Electrochim. Acta* **2010**, *55*, 8461−8465.

(18) Dang, J. X.; Xiang, F.; Gu, N. Y.; Zhang, R. B.; Mukherjee, R.; Oh, I. K.; Koratkar, N.; Yang, Z. Synthesis and Electrochemical Performance Characterization of Ce-Doped $Li_3V_2(PO_4)_3/C$ as Cathode Materials for Lithium-Ion Batteries. *J. Power Sources* **2013**, *243*, 33−39.

(19) Kuang, Q.; Zhao, Y. M.; An, X. N.; Liu, J. M.; Dong, Y. Z.; Chen, L. Synthesis and Electrochemical Properties of Co-Doped $Li_3V_2(PO_4)_3$ Cathode Materials for Lithium-Ion Batteries. *Electrochim. Acta* **2010**, *55*, 1575−1581.

(20) Ren, M. M.; Zhou, Z.; Li, Y. Z.; Gao, X. P.; Yan, J. Preparation and Electrochemical Studies of Fe-Doped $Li_3V_2(PO_4)_3$ Cathode Materials for Lithium-Ion Batteries. *J. Power Sources* **2006**, *162*, 1357−1362.

(21) Li, H. Q.; Zhou, H. S. Enhancing the Performances of Li-Ion Batteries by Carbon-Coating: Present and Future. *Chem. Commun.* **2012**, *48*, 1201−1217.

(22) Choi, M. S.; Kim, H. S.; Lee, Y. M.; Jin, B. S. Enhanced Electrochemical Performance of $Li_3V_2(PO_4)_3$/Ag-Graphene Composites as Cathode Materials for Li-Ion Batteries. *J. Mater. Chem. A* **2014**, *2*, 7873−7879.

(23) Zhang, L. L.; Liang, G.; Peng, G.; Zou, F.; Huang, Y. H.; Croft, M. C.; Ignatov, A. Significantly Improved Electrochemical Performance in $Li_3V_2(PO_4)_3/C$ Promoted by SiO_2 Coating for Lithium-Ion Batteries. *J. Phys. Chem. C* **2012**, *116*, 12401−12408.

(24) Bates, J. B.; Dudney, N. J.; Gruzalski, G. R.; Zuhr, R. A.; Choudhury, A.; Luck, C. F.; Robertson, J. D. Fabrication and Characterization of Amorphous Lithium Electrolyte Thin Films and Rechargeable Thin-Film Batteries. *J. Power Sources* **1993**, *43*, 103−110.

(25) Song, X. Q.; Jia, M. Y.; Chen, R. F. Synthesis of Li_3VO_4 by the Citrate Sol-Gel Method and its Ionic Conductivity. *J. Mater. Process. Technol.* **2002**, *120*, 21−25.

(26) Delmer, O.; Maier, J. On the Chemical Potential of a Component in a Metastable Phase-Application to Li-Storage in the RuO_2-Li System. *Phys. Chem. Chem. Phys.* **2009**, *11*, 6424−6429.

(27) Yang, C. C.; Kung, S. H.; Lin, S. J.; Chien, W. C. $Li_3V_2(PO_4)_3/C$ Composite Materials Synthesized Using the Hydrothermal Method with Double-Carbon Sources. *J. Power Sources* **2014**, *251*, 296−304.

(28) Iwasaki, Y.; Izumi, A.; Tsurumaki, H.; Namiki, A.; Oizumi, H.; Nishiyama, I. Oxidation and Reduction of Thin Ru Films by Gas Plasma. *Appl. Surf. Sci.* **2007**, *253*, 8699−8704.

(29) Qadir, K.; Joo, S. H.; Mun, B. S.; Butcher, D. R.; Renzas, J. R.; Aksoy, F.; Liu, Z.; Somorjai, G. A.; Park, J. Y. Intrinsic Relation Between Catalytic Activity of CO Oxidation on Ru Nanoparticles and Ru Oxides Uncovered with Ambient Pressure XPS. *Nano Lett.* **2012**, *12*, 5761−5768.

(30) Chen, Y. S.; Zhang, D.; Bian, X. F.; Bie, X. F.; Wang, C. Z.; Du, F.; Jang, M.; Chen, G.; Wei, Y. J. Characterizations of the Electrode/Electrolyte Interfacial Properties of Carbon Coated $Li_3V_2(PO_4)_3$ Cathode Material in $LiPF_6$ Based Electrolyte. *Electrochim. Acta* **2012**, *79*, 95−101.

(31) Zhang, S.; Wu, Q.; Deng, C.; Liu, F. L.; Zhang, M.; Meng, F. L.; Gao, H. Synthesis and Characterization of Ti−Mn and Ti−Fe Codoped $Li_3V_2(PO_4)_3$ as Cathode Material for Lithium Ion Batteries. *J. Power Sources* **2012**, *218*, 56−64.

(32) Rui, X. H.; Ding, N.; Liu, J.; Li, C.; Chen, C. H. Analysis of the Chemical Diffusion Coefficient of Lithium Ions in $Li_3V_2(PO_4)_3$ Cathode Material. *Electrochim. Acta* **2010**, *55*, 2384−2390.